Reduced Graphene Oxide Electrolyte-Gated Transistor Immunosensor with Highly Selective Multiparametric Detection of Anti-Drug Antibodies

Matteo Sensi, Rafael Furlan de Oliveira, Marcello Berto, Marina Palmieri, Emilio Ruini, Pietro Antonio Livio, Andrea Conti, Marcello Pinti, Carlo Salvarani, Andrea Cossarizza, Joan M. Cabot, Jordi Ricart, Stefano Casalini, María Begoña González-García, Pablo Fanjul-Bolado, Carlo Augusto Bortolotti, Paolo Samorì, and Fabio Biscarini*

The advent of immunotherapies with biological drugs has revolutionized the treatment of cancers and auto-immune diseases. However, in some patients, the production of anti-drug antibodies (ADAs) hampers the drug efficacy. The concentration of ADAs is typically in the range of 1–10 pM; hence their immunodetection is challenging. ADAs toward Infliximab (IFX), a drug used to treat rheumatoid arthritis and other auto-immune diseases, are focussed. An ambipolar electrolyte-gated transistor (EGT) immunosensor is reported based on a reduced graphene oxide (rGO) channel and IFX bound to the gate electrode as the specific probe. The rGO-EGTs are easy to fabricate and exhibit low voltage operations (≤ 0.3 V), a robust response within 15 min, and ultra-high sensitivity (10 aM limit of detection). A multiparametric analysis of the whole rGO-EGT transfer curves based on the type-I generalized extreme value distribution is proposed. It is demonstrated that it allows to selectively quantify ADAs also in the co-presence of its antagonist tumor necrosis factor alpha (TNF-α), the natural circulating target of IFX.

1. Introduction

The development of therapies based on biological drugs has represented a veritable cornerstone in the treatment of diverse pathologies, from cancer to auto-immune diseases. The extensive use of chimeric monoclonal antibody Infliximab (Remicade, termed from now on IFX)[1,2] to treat auto-immune diseases like psoriasis, Crohn's disease, and rheumatoid arthritis, is a successful example.[1,3] The Fab fragment of IFX binds and inactivates the proinflammatory cytokine tumor necrosis factor-alpha (TNF-α), inhibiting its interaction with the specific cell receptors thereby decreasing inflammation, which is a hallmark of autoimmune diseases.[4] However, the prolonged treatment with IFX and, in general, with biological drugs, can induce in some patients the development of anti-drug antibodies (ADAs) that by sequestering the drug, make the treatment ineffective. Additionally, the level of ADAs toward IFX (termed from now on ATIs–Antibodies Toward Infliximab) found in patient serum is very low, ranging from 1–10 pM, thereby making their quantification challenging. Rapid and sustainable diagnostic tools for ATI detection at Point of Care (POC) are key to bourgeon personalized medicine in a variety of clinical fields.

M. Sensi, M. Berto, M. Palmieri, E. Ruini, M. Pinti, C. A. Bortolotti, F. Biscarini
Department of Life Sciences
University of Modena and Reggio Emilia
via Campi 103, Modena 41125, Italy
E-mail: fabio.biscarini@unimore.it
R. F. de Oliveira, P. A. Livio, S. Casalini, P. Samorì
Université de Strasbourg, CNRS, ISIS
8 allée Gaspard Monge, Strasbourg 67000, France

R. F. de Oliveira
Brazilian Nanotechnology National Laboratory (LNNano)
Brazilian Center for Research in Energy and Materials (CNPEM)
Campinas 13083-970, Brazil

A. Conti
Dermatology Unit
Surgical
Medical
and Dental Department of Morphological Sciences Related to Transplant
Oncology and Regenerative Medicine
University of Modena and Reggio Emilia
via del Pozzo 71, Modena 41125, Italy

C. Salvarani
Rheumatology Unit
University of Modena and Reggio Emilia
Medical School Azienda Ospedaliero-Universitaria Policlinico di Modena
via del Pozzo 71, Modena 41125, Italy

ADVANCED
SCIENCE NEWS

www.advancedsciencenews.com

**ADVANCED
MATERIALS**

www.advmat.de

The detection of ATI is mostly performed with laboratory tests, ELISA kits, and lateral-flow assays; the latter are hardly suitable for quantification.[5] Label-free ATI detection was achieved with surface plasmon resonance (SPR),[6–8] whose technical complexity makes it rarely used in POC settings. Electrolyte-Gated Transistors (EGTs) are ideally suited for POC immunosensing because of their rapid response, safe low-voltage operations, disposable items, and low-cost manufacturing.[10–13] Recently, we demonstrated the first label-free ADAs immunosensors with electrolyte-gated organic field-effect transistors (EGOFETs) where the drug (Nivolumab, a drug targeted to melanoma) was used as the specific biorecognition element in the device. The EGOFET exhibited high sensitivity (10^{11} M^{-1} at 10^{-12} M ADA) and theoretical limit of detection (LOD) in the fM range required for ADA.[9] The use of organic solvents for processing the organic semiconductor is a hurdle for scaling up the sensing platform.

One of the most attractive materials for EGT-based biosensors is reduced graphene oxide (rGO)[14–18] due to both its outstanding electronic properties approaching those of graphene (conductivity > 1000 S cm^{-1}), coupled to an excellent processability of aqueous graphene oxide (GO) dispersions.[19] Most of the rGO-EGT biosensors in the literature exploit the oxidized carbon groups present in rGO to tether recognition elements directly onto the rGO surface for the specific detection of the target analyte.[16,20–22] The binding of the target analyte on the functionalized transistor channel induces a change in the device current[16,20,23] (often monitored vs time) and/or a shift of the voltage at the charge neutrality point (V_{CNP}).[24] One disadvantage of direct functionalization of the rGO surface is the difficult technological control of available surface oxygen-containing moieties, whose density depends on the GO reactions and processing.

Here, we graft the biological drug IFX on the device gate electrode and exploit the whole ambipolar response (namely, both hole and electron current modulation)[25–27] of rGO-EGTs to demonstrate an ultra-sensitive, highly specific, and selective immunosensor for ATIs. EGTs were manufactured by fast and scalable laser scan ablation on plastic substrates. The rGO channel was obtained by in situ electrochemical GO reduction in an aqueous solution and in the absence of toxic chemicals. We show that the standard analysis of the transfer curve versus concentra-

tion of the target analyte does not allow us to adequately differentiate the dose curves of ATI and TNF-α, being the designed target for IFX. Therefore, to unravel the device selectivity, we propose a multiparametric analysis of the immunosensor transfer curves renormalized to the minimum current point, the so-called charge neutrality point CNP, as a function of the distance potential from the CNP voltage. Our method exploits all the experimental points of the transfer curve, and yields dose curves that on the one hand are independent of the choice of displacement voltage, and on the other hand, are statistically distant from the dose curve of TNF-α. Our rGO sensor attains LOD for ATI as low as 10 aM. The demonstrated device sets the basis for a low-cost and disposable POC diagnostic platform for anti-drug antibodies.

2. Results and Discussion

2.1. Device Characterization and Optimization

The device consists of two plastic substrates fabricated separately: one is patterned with a planar Au gate (G) electrode (20 nm-thick) whose geometrical area is 12.25 mm,[2] and the other with a pair of Au source (S) and drain (D) interdigitated electrodes (IDEs, 20-nm thick) exhibiting a channel width and length ratio $W/L = 100$. The rGO channel is obtained by the electrochemical reduction of GO thin film deposited on the IDEs (Figure S1, Supporting Information). Once the gate and IDEs substrates are assembled, the layout appears as in **Figure 1**a, where electrodes are bridged by a 40 µL droplet of 50 mM PBS buffer at pH 7.4. Separated gate and IDEs substrates layout allow us to repeat measurements with either the same rGO-coated IDEs or the same functionalized gate, to assess the robustness of our sensor. Details on the device fabrication are reported in the Experimental section.

Figure 1b shows a characteristic rGO-EGT transfer curve I_{DS} versus V_{GS} exhibiting ambipolar behavior, with hole (p-type) and electron (n-type) conduction at negative and positive V_{GS} values from the charge neutrality point V_{CNP} featuring the lowest current $I_{DS,CNP}$ occurs. The transconductance (dI_{DS}/dV_{GS}) of the rGO-EGT is in the order of several µS.[25–28]

We systematically investigated the device operations and architecture to optimize the rGO-EGT response. First, we measured the transfer characteristics of devices with coplanar gate electrodes of different areas and the same transistor channel. Small gate electrodes (featuring 1 mm^2 geometrical area and 0.72 ± 0.15 mm^2 electrochemically active surface area ESA, Figure S3, Supporting Information) and large gate electrodes (12.25 mm^2 geometrical area and 7.4 ± 1.2 mm^2 ESA) were used. Devices with large gate electrodes exhibit higher I_{DS} compared to those having smaller gate areas (Figure S2, Supporting Information). This is the result of the enhancement of areal charge carrier density in the rGO channel when a larger gate area, hence a larger gate capacitance, is used.[29] Also the curvature of the transfer curve at V_{CNP} is greater for the large gate electrode compared to the small one.

Aiming at extracting the descriptors of the whole transfer curve we fit the curves in the entire V_{GS} range with the following function termed Gumbel distribution or type-I generalized extreme value distribution[30]

$$I_{DS}\ (z) = I_{DS,\infty} + A \cdot exp^{[-exp^{(-z)}+1-z]} \tag{1}$$

A. Cossarizza
Department of Medical and Surgical Sciences for Children and Adults
University of Modena and Reggio Emilia
Via Campi 287, Modena 41125, Italy

J. M. Cabot, J. Ricart
Leitat Technology Center
Innovació 2, Barcelona 08225, Spain

S. Casalini
Dipartimento di Scienze Chimiche University of Padova
via Marzolo 1, Padova 35131, Italy

M. B. González-García, P. Fanjul-Bolado
Metrohm DropSens
S.L. Vivero Ciencias de la Salud
C/Colegio Santo Domingo de Guzmán s/n
Oviedo 33010, Spain

F. Biscarini
Center for Translational Neurophysiology
Istituto Italiano di Tecnologia
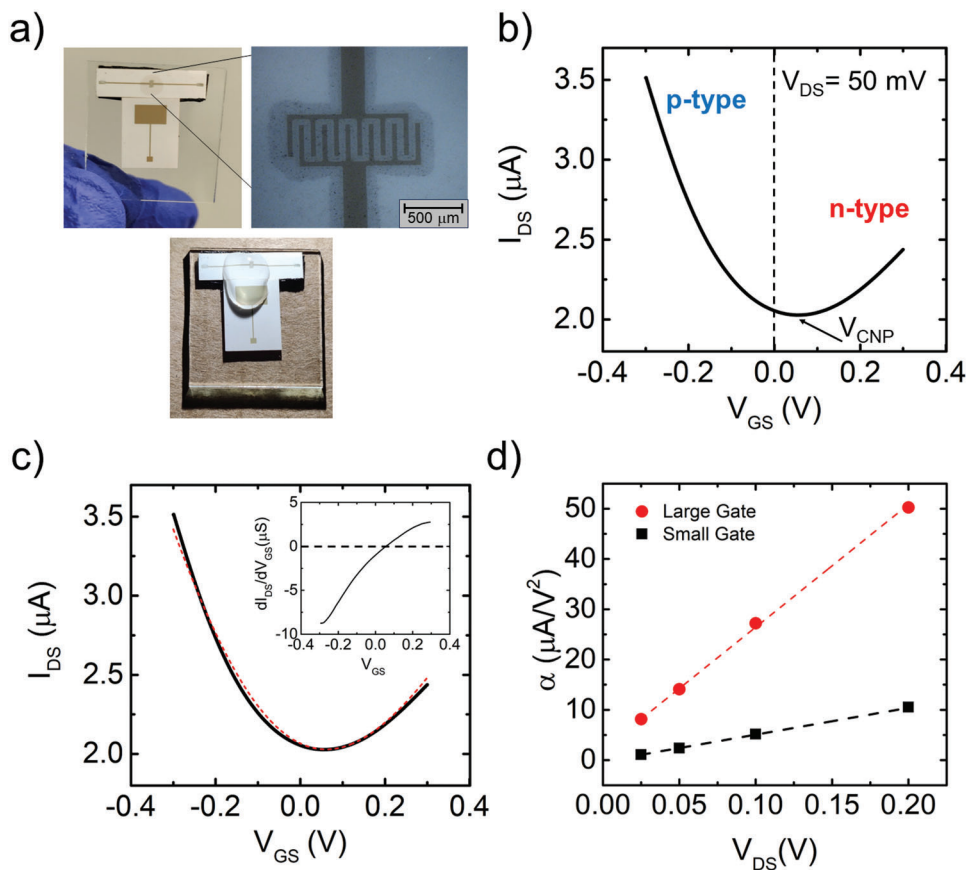Via Fossato di Mortara 17–19, Ferrara 44121, Italy

**ADVANCED
SCIENCE NEWS**
www.advancedsciencenews.com

**ADVANCED
MATERIALS**
www.advmat.de

Figure 1. a) Photograph of the rGO-EGT device made of two electrode substrates (white rectangles with gate and source/drain IDEs). The dark-field optical microscopy image of the rGO-coated IDEs evidence the halo generated upon the GO film deposition and darker color on the electrodes due to electrochemical reduction to rGO. The third image shows the electrolyte drop covering both gate and channel regions for the measurement. b) Device transfer curve measured with a large gate electrode (12.5 mm^2 area) and 40 µL drop of 50 mM PBS at pH 7.4. V_{CNP} is the voltage at the charge neutrality point, V_{GS} the gate-source voltage, I_{DS} and V_{DS} are the drain-source current and voltage. c) Transfer curve fitted (red dashed line) with Equation (1). The inset shows the dI_{DS}/dV_{GS} versus V_{GS} curve obtained by numerical differentiation of the experimental transfer curve. The horizontal dashed line is the zero-derivative at CNP. d) Coefficient α (from the best fit with Equation (1) versus V_{DS} for large (red markers) and small (1 mm^2, black markers) gate electrodes. Dashed lines are the result of a linear fit.

The fitting parameters are V_{CNP}, $I_{DS,\infty}$, A, ν. The parameter $I_{DS,\infty}$ is the current value for $z \to \infty$. There, $z = \frac{V_{GS} - V_{CNP}}{\nu}$, the current at the CNP is $I_{DS, CNP} = I_{DS,\infty} + A$. The function Equation (1) reproduces the parabolic trend near the minimum $V_{GS} \approx V_{CNP}$, viz.

$$I_{DS} \approx \alpha \cdot \left(V_{GS} - V_{CNP} \right)^2 + I_{DS, CNP} \qquad (2)$$

where the curvature near the CNP is $2\alpha = -\frac{A}{\nu^2}$. This implies that A is always negative for rGO-EGTs. Equation (1) also predicts the linear trend of the transfer curve away from the minimum at $\frac{V_{GS} - V_{CNP}}{\nu} \approx \pm 1$ where the first derivative of Equation (1) exhibits the largest absolute values (viz. a maximum and a minimum, respectively) for V_{GS} larger (n-type branch) and smaller (p-type branch) than V_{CNP}. Thus, the linear approximation to the transfer curve holds strictly at the inflection points of Equation (1) (zero curvature). An example of the fit with Equation (1) is shown in Figure 1c. We numerically differentiate each transfer curve to yield dI_{DS}/dV_{GS}, which would be the transconductance g_m at the

inflection points. However, as the fit parameters reveal, these are not always accessible in the voltage range of operations, hence we approximate the two g_m values for holes and electrons with the values at the experimental endpoints (in Figure 1c $V_{GS} = -0.3$ V and $V_{GS} = 0.3$ V).

We exploit this analysis to assess the effect of gate electrode size on the curvature. The rGO-EGT transfer characteristics acquired at different positive V_{DS} show the linear trend of α versus V_{DS} (Figure 1d), where the large electrode exhibits larger α values and a steeper slope than the small gate electrode. The positive V_{DS} also causes a positive V_{CNP} shift,[31] more pronounced for the small gate electrode. This effect is evidenced in Figure S2c,d (Supporting Information), where the normalized curves are obtained from those in Figure S2a,b (Supporting Information) by subtracting $I_{DS,CNP}$, then dividing by the current value at $V_{GS} = -0.3$ V. For the large gate electrode, V_{CNP} is weakly affected by V_{DS}, and the current hysteresis is negligible. Conversely, for the small gate electrode V_{CNP} is substantially shifted by V_{DS}, and the current hysteresis is pronounced. Both the hysteresis and the V_{CNP} shift are ascribed to the electrolyte ions mobility and adventitious

ADVANCED
SCIENCE NEWS

www.advancedsciencenews.com
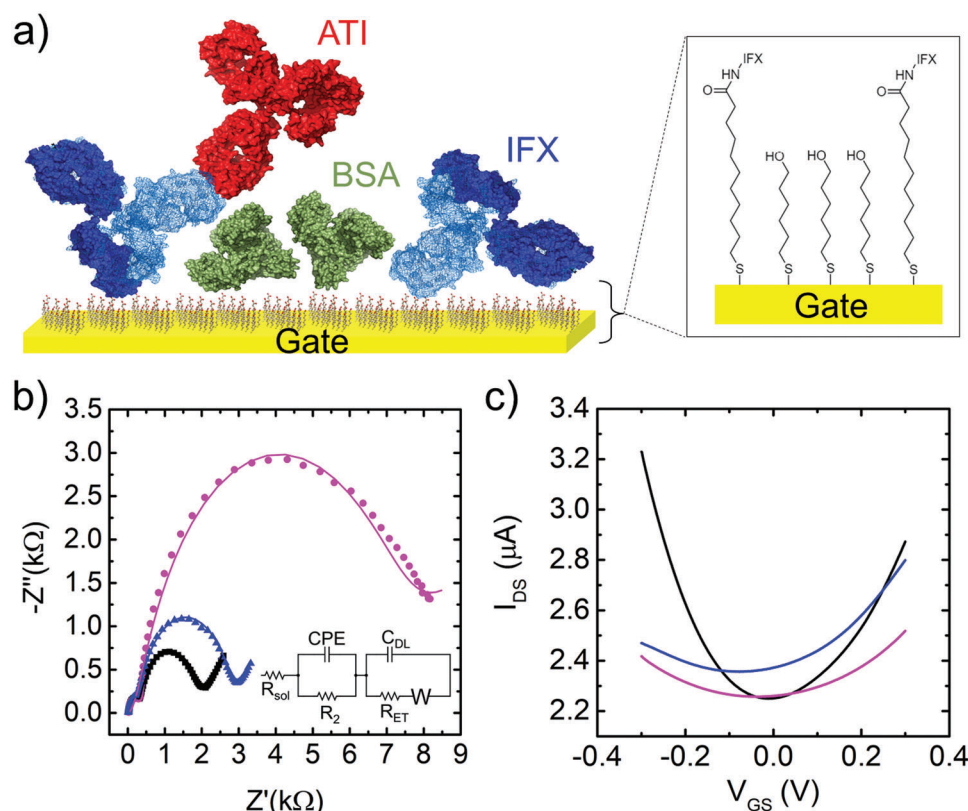
ADVANCED
MATERIALS

www.advmat.de

Figure 2. a) Schematic drawing of the functionalized gate. The crystallographic structure of Infliximab was obtained from the PDB file 4G3Y, while for the ATI we used the IgG1 PDB file 1IGY. The inset shows the MUA/MCH self-assembled monolayer (SAM) on the gate bound to a primary amine of Infliximab (IFX). b) Nyquist plots (-Z'' vs Z') from EIS acquired on the large gate electrode upon each functionalization step: black squares for Au electrode, magenta dots for MUA/MCH and blue triangles for IFX+ETA. The lines are the results of the fitting with the representative electrical circuit (inset). c) rGO-EGT transfer characteristics recorded at each functionalization step on the large gate electrode at V_{DS} = 50 mV in 50 mM PBS pH 7.4. The color-code is the same of panel b.

p-doping, that are both affected by V_{DS} and V_{GS} sweeping rate.[29] Based on these observations, we infer that large gate electrode makes the EGT more sensitive and more stable, which are important features for optimum immunosensor response.

2.2. Gate Biofunctionalization

To endow the gate specificity for the detection of ATI, we immobilized the drug (Infliximab, IFX) on the device gate electrode to act as a bioreceptor (see Experimental Section). The schematic drawing of the assembly for biorecognition is shown in **Figure 2**a.

First, a self-assembled monolayer (SAM) made of 1:3 mixture of mercaptoundecanoic acid (MUA) and 6-mercaptohexanol (MCH) is assembled on the Au gate electrode. Then, upon activation with *N*-(3-dimemethylaminopropyl)-*N'*-ethylcarbodiimide/*N*-hydroxysuccinimide (EDC/NHS) crosslinker, the carboxylic groups of the SAM are covalently bound to an amine group exposed by IFX. The unreacted intermediates are finally blocked by ethanolamine (ETA) 0.5 M. We monitored the immobilization steps by electrochemical impedance spectroscopy (EIS) measurements in presence of

a $K_3[Fe(CN)_6]$ redox probe. The Nyquist plot in Figure 2b displays a significant increase in the impedance of the bare gate electrode after MUA/MCH functionalization step, followed by a substantial decrease upon the binding of IFX and ETA on the SAM.[32] We extracted the electrical double-layer capacitance (C_{DL}) and the electron transfer resistance (R_{ET}) after the gate functionalization. On the bare Au, C_{DL} is large (≈10 µF) and R_{ET} is small (1 kΩ). Upon functionalization of the gate electrode with the SAM, C_{DL} decreases to ≈6 µF while R_{ET} increases to 7 kΩ, which may be regarded as the SAM adding a capacitance and a resistance in-series to the gate electrode representative circuit (Figure 2b inset). The tenfold increase of R_{ET} is expected because of the enhanced distance for electron transfer due to the compact SAM as well as the electrostatic repulsion of the carboxylic end groups toward the $[Fe(CN)_6]^{3-}$ ions. Upon immobilization of IFX, C_{DL} remains constant while R_{ET} significantly decreases (from 7 to ≈2 kΩ). This behavior can be explained in view of the formation of amide bonds with IFX and ETA, which decreases the electrostatic repulsion between the surface and the redox probe. Since the distance for electron transfer also increases, the decreased resistance suggests the occurrence of a structural re-organization within the SAM (likely yielding a decreased compactness) upon the EDC/NHS reaction, in agreement with earlier observations.[31] Thus, EIS provides clear evidence that

**ADVANCED
SCIENCE NEWS**

www.advancedsciencenews.com

**ADVANCED
MATERIALS**

www.advmat.de

the functionalization with IFX and ETA was successful, although we cannot quantify the areal density of the ATI-biorecognition IFX element.

Then, we look at the rGO-EGT transfer curves, displayed in Figure 2c. The presence of the MUA/MCH SAM on the gate electrode decreases the curvature and reduces the current modulation induced by V_{GS} (both for p- and n-type conduction), while $I_{DS,CNP}$ remains nearly the same. Upon a large number of gate sweep cycles, the SAM-functionalized gate remains stable, meaning that we do not observe a marked difference between successive transfer curves. The absence of the drift toward the transfer characteristics of bare Au tells us that the SAM is stable, and the electrode does not recover to the state of bare gold upon repeated cycles. The immobilization of IFX and ETA induces a slight negative shift $\Delta V_{CNP} = -30$ mV. When IFX is grafted on the SAM (blue curve in Figure 2d) the transfer curve still exhibits a well-balanced n- and p-type responses, with curvature comparable to those of the transfer curve of MUA/MCH/Au together with a slight current increase of $I_{DS,CNP}$. We infer that the behavior of the rGO-EGT transfer curves is consistent with the EIS results and that the trend of the transfer curves is a viable gauge for the successfulness of the functionalization steps.

2.3. ATI Detection

The working mechanism of the sensor is most likely similar to that of the electrolyte-gated transistor: the modulation of the gate voltage displaces ions at both gate/electrolyte and rGO channel/electrolyte interfaces, to create two non-equilibrium interfacial ion distributions (that at zeroth order might be regarded as electrical double layers). In this specific case, being rGO a 2D material with high surface area and permeable to ions,[33] the excess of ions (of the same charge as the gate voltage applied) may adsorb at the surface or intercalate in between the rGO sheets, in both cases causing a change of the carrier density (either holes or electrons depending on the bias). Whether this may be due to capacitive coupling or strong perturbation/interaction of the ions with the pi-system of rGO is difficult to be unambiguously established. The sensitivity of the EGTs devices is, from literature experiments to date as well as in our everyday evidence, apparently not limited by Debye length in the recognition event. Hypotheses were made by G. Palazzo and L. Torsi[34] about the role of Donnan capacitance in controlling the effective capacitance. We believe that the observed behavior arises from the displacement and reorganization of water molecules and solvated ions in the vicinity of the recognition site, which propagates and interacts with water molecules and ions all the way down to the gate electrode surface.

The detection of ATI was performed by measuring the device transfer characteristics in 50 mM PBS, pH 7.4, enriched with 0.1 mg mL^{-1} bovine serum albumin (BSA) after the gate electrode was incubated in spiked solutions of the same buffer containing an increasing concentration of ATI, for 20 min. The addition of BSA is standard in ELISA protocols. After each incubation, the gate electrode is rinsed to remove physisorbed ATIs, and then the whole device is measured. The presence of BSA in the buffer serves to decrease the non-specific ATI binding on the gate electrode and, at the same time, makes the buffer more similar to the patient's samples where albumin is the most abundant protein.

As shown in **Figure 3**a, the gate exposure to increasing ATI concentrations, from 1 fM to 10 nM, induces a decrease of I_{DS} in the n-type branch of the curve together with a monotonic shift of V_{CNP} toward more positive V_{GS}. The I_{DS} of the p-type branch of the transfer curve increases but the branches bundle into a set of curves, which makes it difficult to assess the effect of concentration.

We initially focus on the n-type branch at V_{GS} more positive than V_{CNP}. We build the dose curve for ATI by measuring the I_{DS} at the highest V_{GS} value (+0.3 V) on the n-type branch of the device transfer curve. As commonly done in most papers employing EGOFET sensors works, the sensing signal S is the relative variation of current $S_{I_{DS}} = -\{\frac{I_{DS}([ATI])-I_{DS,0}}{I_{DS,0}}\}$ taken at a given V_{GS} (here = +0.3 V), where I_{DS} ([ATI]) is the device I_{DS} current at molar concentration [ATI], while $I_{DS,0}$ is the device I_{DS} current measured in the absence of ATI. Figure 3b shows the S trend versus ATI concentrations (red squares). The immunosensor signal S exhibits a logarithmic increase across the range 0.02–0.2 for ATI concentration spanning over 7 orders of magnitude, from 1 fM to 10 nM. The theoretical LOD found amounts to 10 aM (see Experimental Section for definition). This analysis accounts only for a few points extracted from the transfer curves.

In patients' plasma, the pathological circulating concentration of TNF-α is $\approx$1 pM.[35] To assess the possible interference of TNF-α in our sensor, we exposed the functionalized gate to the same ATI solutions as above but having constant [TNF-α] = 1 pM. As shown by the circles in Figure 3b, S is slightly offset compared to that comprising only ATI (red squares). The S offset induced by TNF-α is not surprising since TNF-α is the biological target of IFX. In fact, our device is not designed to be specific in real samples, albeit we may expect different interaction pattern and binding free energy toward IFX with respect to ATI. Then, an independent quantification of TNF-α is necessary to correct the calibration curve by subtracting the TNF-α additive contribution to S. For this reason, we investigated the response to TNF-α in the absence of ATI. The experiment was performed by diluting TNF-α in 50 mM PBS pH 7.4 and 0.1 mg mL^{-1} BSA and using the same gate functionalization. The TNF-α dose curve in Figure 3b (red triangles) shows that the binding of TNF-α to the IFX-functionalized gate produces a S_{IDS} signal comparable to the S_{IDS} of ATI for concentrations above 10 pM, which is within the relevant pathophysiological range for TNF-α. The steeper slope of the TNF-α curve suggests that binding constant of TNF-α to IFX is larger than that of ATI to IFX. The plateau onset of the red curve above 1 pM is consistent with the dissociation constant for IFX/TNF-α estimated in the literature (44 pM).[36] Finally, we performed control experiments where the device gate electrode is functionalized with the SAM, EDC/NHS, and ETA but without grafting IFX. The gate was exposed to solutions where ATI is in co-presence with 1 pM TNF-α. The red diamonds in Figure 3b show that S_{IDS} possess an insignificant magnitude, confirming the immunosensor selectivity toward the molecular targets of IFX.

The analysis described above and relative to Figure 3b is alike the procedure carried out in unipolar EGOFET sensors,[37–41] in the case of rGO only the n-type branch appears viable for

**ADVANCED
SCIENCE NEWS**

www.advancedsciencenews.com
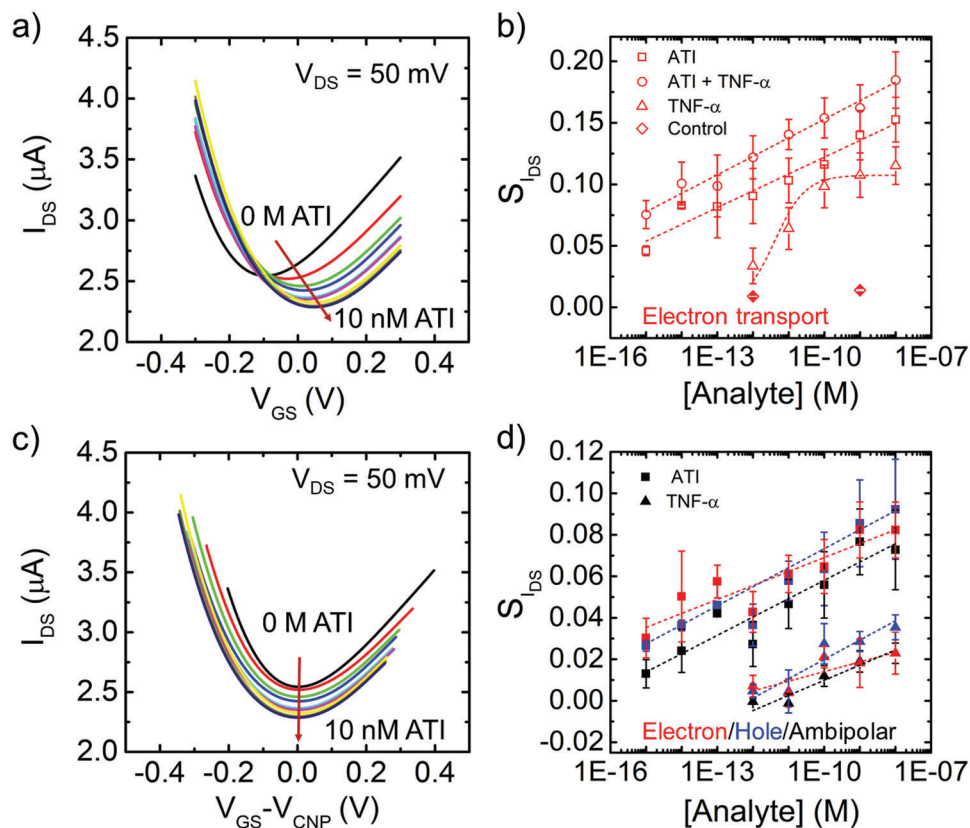
**ADVANCED
MATERIALS**

www.advmat.de

Figure 3. ATI detection. a) rGO-EGT transfer curves acquired after incubating the IFX-functionalized device gate electrode to increasing concentrations of ATI in presence of BSA and TNF-α. $V_{DS} = 50$ mV; b) Dose curves from current signal S_{IDS} obtained at $V_{GS} = +0.3$ V and $V_{DS} = 50$ mV for the detection of ATI (squares), ATI+TNF-α (circles), TNF-α (triangles). The response from the control experiment (diamonds) was obtained by exposing two devices without IFX on the gate (SAM blocked with ETA) to ATI with 1 pM TNF-α in solution. c) Offset transfer curves obtained by horizontal shift of each curve in panel a by its V_{CNP}. V_{CNP} is obtained by fitting with Equation (1). d) Dose curves for ATIs (circles) and TNF-α (triangles) obtained from signal S_{IDS} at constant $V_{GS}-V_{CNP}$ values: -0.2 V (hole current, blue), 0 V (ambipolar current, black) and $+0.2$ V (electron current, red). In b and d the error bars are the standard error SEM of three datasets for TNF-α, six datasets for ATI, and five datasets for ATI+TNF-α obtained with independent gate electrodes and rGO channels. An example of the transfer curves obtained with TNF-α is shown in Figure S4 (Supporting Information).

extracting a signal. As we showed, the analysis with the signal from n-type branch alone does not enable us to discriminate ATI and TNF-α in a relevant concentration range. By constructing the dose curve with the concentration-dependent values at a precise V_{GS} value, on the one hand, we introduce an operator dependent bias, on the other hand we disregard the information by the whole curve and specifically by the ambipolar response of rGO. Starting from these considerations, to overcome these limitations we explored an alternative approach to the analysis of the transfer curve that allows us to access the whole information contained in the rGO-EGT ambipolar behavior. Thus, we propose an innovative multi-parametric analysis that applies to the whole rGO-EGT transfer curve, specifically, it extracts information from p-type and n-type branches and from CNP, with no a priori bias.

First, we fit Equation (1) to each transfer curve at same ATI concentration. The values for the parameters V_{CNP}, α, and $I_{DS,CNP}$ are extracted and averaged to yield their mean values and their respective rms standard deviations, the latter then being converted into the standard error of the mean (SEM). In Figure 3c, the transfer curves are horizontally aligned by the offset $V_{GS_-} V_{CNP}$. The constant term $I_{DS,CNP}$, also sensitive to [ATI], staggers the curves

one with respect to each other. While it is clear that [ATI] affects the minimum current $I_{DS,CNP}$ both the curvature and the slope of the linear regions seem less sensitive to [ATI]. In Figure 3d, we show the dose curves S_{IDS} built this time from the relative differences of current at constant $V_{GS}-V_{CNP}$ in the n-type branch ($V_{GS} > V_{CNP}$ red markers), p-type branch ($V_{GS} < V_{CNP}$ blue markers) and at the CNP ($V_{GS} = V_{CNP}$ black markers). From the comparison with the dose curves extracted at the same value of V_{GS} (as in Figure 3b) the "traditional" EGOFET dose curve is more sensitive only when built out of the electron current, it is equivalent in the case of the ambipolar current, and it is strongly less sensitive for the hole current. Interestingly, the dose curves built with our approach "collapse" into narrower bundles, hence they become effectively independent of the chosen $V_{GS}-V_{CNP}$. Hence, the bias on the choice of V_{GS} for building the dose curve has been lifted. Interestingly, we notice that in this case, differently from Figure 3b where the dose curves of ATI and TNF-α largely overlap, the dose curve of TNF-α (triangles) is always significantly below that of ATI (squares), with its highest value close to the LOD of the dose curves of ATI. Thus, by exploiting the ambipolar character of rGO-EGT, we succeeded in maximizing the difference between the dose curves of ATI and those
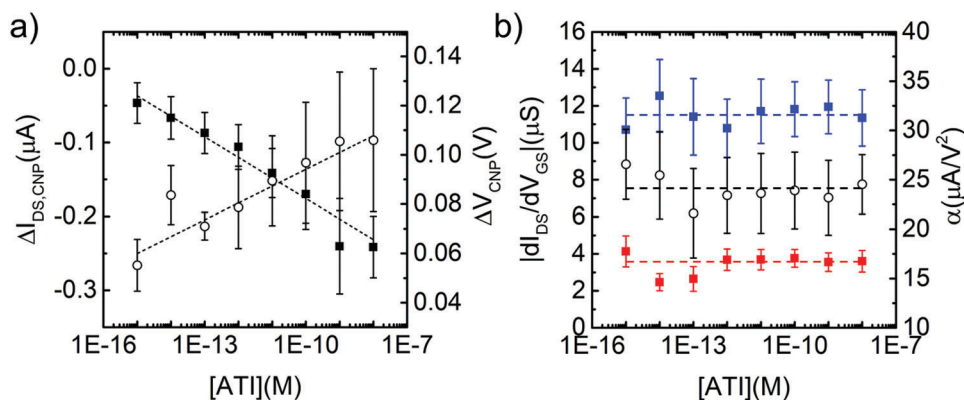
**ADVANCED
SCIENCE NEWS**

www.advancedsciencenews.com

**ADVANCED
MATERIALS**

www.advmat.de

Figure 4. Multiparametric analysis of rGO response. a) $\Delta I_{DS,CNP}$ (black filled squares) and ΔV_{CNP} (empty circles) as a function of the ATI concentration. b) Maximum transconductance of the rGO-EGT for holes (blue squares) and electrons (red squares) conduction, and the parameter α (open circles) as a function of ATI concentration. The lines are the mean values. The datasets used for the analysis are the same reported in Figure 3 for ATI detection curves.

of TNF-α, thereby yielding a threefold enhancement of the ATI signal when compared to that of TNF-α at the same concentration. We conclude that the new data analysis achieves the discrimination of the two antagonist targets of IFX, ATI, and TNF-α, compared to the curves in Figure 3b. This represents a clear advantage offered by the rGO device compared to the unipolar EGOFETs.

2.4. Multiparametric Analysis of the rGO Sensor Response

The approach based on fitting the transfer curves with Equation (1) further enables the possibility to perform a multiparametric analysis of the response, in place of a simple inversion of the current signal versus concentration dose curve to determine the device sensitivity. This is desirable to sort out possible interference or spurious effects. In **Figure 4** we show the trends of the variation of $I_{DS,CNP}$ and V_{CNP} with respect to their values at the charge neutrality point of the device with the reference solution, i.e., $\Delta I_{DS,\,CNP} = I_{DS,CNP,0} - I_{DS,CNP}([ATI])$ and $\Delta V_{CNP} = V_{CNP,0} - V_{CNP}([ATI])$ (Figure 4a), and the (nearly constant) trends of the linear transconductance of holes and electrons, and of the curvature parameter α (Figure 4b).

Interestingly, both $\Delta I_{DS,CNP}$ and ΔV_{CNP} displays a monotonic logarithmic trend upon increasing [ATI], with the current decreasing to smaller values and the V_{CNP} voltage increasing toward more positive values. Hence, both the shift of the minimum current $\Delta I_{DS,CNP}$ and its voltage ΔV_{CNP} are sensitive to ATI concentration, with sensitivity being proportional to $[ATI]^{-1}$. Conversely, both transconductances and curvature parameter appear less sensitive to ATI concentration, and we consider them constant and equal to their mean values ($\pm$standard deviation) $g_{m,h}$ = 11.2($\pm$4.1) μS, $g_{m,e}$ = 3.5($\pm$1.2) μS and α = 11.4($\pm$4.2) μA V^{-2}. The larger transconductance for holes suggest that their mobility is higher than that of electrons. We conclude that the parameters more sensitive to the binding of ATI to IFX anchored at the gate electrode are the minimum current and the voltage at the CNP.

3. Conclusion

In this manuscript, we report on the first reduced graphene oxide-based electrolyte-gated transistor (rGO-EGT) immunosensor for the detection of ADAs. The device is fabricated by laser ablation of the gate (on disposable plastic substrate) and the channel (that can be re-used for different gates). The channel is covered with the solution-processed 2D-material, i.e., GO, which is then reduced to the electroactive rGO by means of an aqueous electrochemical reaction. With our EGT architecture, we achieve good sensitivity and robustness, thereby attaining a theoretical limit of detection as low as 10 aM for antibodies toward Infliximab (ATI). The immunosensor detects ATIs also in presence of interfering agents, namely albumin (non-specific, high concentration) and TNF-α (antagonist of ATI), both commonly found in samples from patients. The dose curves are distinctive for ATI with respect to ATI+TNF-α, and also with respect to TNF-α. The proposed multiparametric analysis of the whole rGO transfer curves versus the displaced $V_{GS-} V_{CNP}$ allows us to build V_{GS}-independent dose curves and to discriminate the dose curves for ATI with respect to that for TNF-α. In perspective, one could impart selectivity by designing a dual gate device, one gate electrode functionalized with the drug, the other with an antibody against TNF-α, and by comparing the concentrations outcoming from the respective dose curves. We found that V_{CNP}, and the minimum current $I_{DS,CNP}$ are most sensitive to [ATI].

The developed protocol is of general applicability for the detection of any ADA of choice, through the controlled functionalization of the gate electrode with the suitably designed probe endowing high selectivity in the recognition process.

Hence, the manufactured device represents a significant step forward in the field of POC as diagnostic tool for personalized medicine that is enabled through the fine control of the rGO materials properties.

4. Experimental Section

Biomolecules and Chemicals: Infliximab (Remicade) was provided in saline solution. Human Anti-Infliximab monoclonal antibodies were

purchased from BioRad (Clone AbD19370_hIgG1), resuspended in PBS 50 mM pH 7.4 and stored at −20 °C.

Bovine Serum Albumin, TNF-α, *N*-(3-dimemethylaminopropyl)-*N*'-ethylcarbodiimide , ethanol, ethanolamine, 6-mercaptohexanol, 11-mercaptoundecanoic acid, *N*-hydroxysuccinimide , sulfuric acid, and phosphate salts were purchased from Merk–Sigma–Aldrich.

Device Fabrication: Polyethylene terephthalate (PET) substrates (160 µm thick) sputter-coated with 20 nm Au layer were ablated with a Nd:YAG laser (532 and 1064 nm wavelengths, adjustable power) in an automated laser scribing station (Rofin, Germany) at the laboratories of Metrohm Dropsens (Oviedo, Spain). manufactured Au gate electrodes with two dimensions (1 and 12.25 mm^2 area each) were manufactured, and a pair of interdigitated electrodes (IDEs) exhibiting 12 fingers, channel width (W) and length (L) ratio of $W/L = 100$. The gate and IDE substrates were fixed onto an adhesive layer to prevent sliding during the electrical measurements. This keeps gate and IDEs 4.5 mm apart.

Graphene Oxide (GO) Deposition and Reduction: Prior to use, the device ablated electrodes were cleaned individually with iso-propyl alcohol, and water, and dried under a gentle flow of N$_2$. Poly(diallylmethylammonium chloride) (PDDA) from Sigma–Aldrich was employed as an adhesive layer to promote the GO fixation onto the device channel region. For this purpose, a PDDA solution prepared in water (1% w/w) and containing 0.5 M of NaCl was casted (20 µL) onto the IDEs for 15 min and rinsed thoroughly in water afterward. A GO suspension in water having 0.4 mg mL^{-1} prepared from a stock commercial solution from Graphene a (4 mg mL^{-1}, monolayer content >95%, lateral flake size < 10 µm), sonicated for 1 min prior to use, was casted onto the PDDA-coated IDEs for 30 min. After that, the functionalized IDE region was rinsed copiously with water and dried under N$_2$ flow to obtain a PDDA/GO bilayer. The casting steps were carried out inside a sealed glassware having a small water reservoir to create a saturated humidity environment, which prevents rapid water evaporation during the PDDA and GO assembly, avoiding inhomogeneous film formation. The electrochemical reduction of the GO film adsorbed onto the PDDA-functionalized IDEs was carried out as described elsewhere.[25] The coated IDEs were short-circuited to act as the working electrode (WE) in the electrochemical setup using a Metrohm Autolab PGSTAT 204 potentiostat/galvanostat. A drop of 50 µL of water was positioned onto the GO-coated IDE region and a polycrystalline Au plate (area ≈0.031 cm^2) sitting atop of the drop was used as the counter (CE)/reference (RE) single electrode. The GO reduction was achieved by cyclic voltammetry, sweeping WE potential from 0 to −2.8 V at a scan rate of 100 mVs^{-1} for a total of 4 cycles. Figure S1 (Supporting Information) depicts the device fabrication steps from PDDA/GO film deposition to the GO electrochemical reduction.

Gate Electrode Functionalization and Electrochemical Characterization: To generate the biorecognition surface, the gate was i) incubated in a vial with 1 mM mercapto-undecanoic acid and 3 mM 6-mercaptohexanol in ethanol overnight; ii) after rinsing with ethanol and water, the gate was covered with a 40 µL drop of an aqueous solution of 100 mM *N*-(3-dimemethylaminopropyl)-*N*'-ethylcarbodiimide and 25 mM *N*-hydroxysuccinimide for 30 min; iii) the solution was removed and replaced with a 40 µL drop of 2.7 µM Infliximab (pI 7.6)[42] in 50 mM PBS, pH 7.4, for 2 h 30 min; iv) the gate was rinsed with 50 mM PBS and covered with a drop of 0.5 M ethanolamine aqueous solution for 30 min; v) the gate was rinsed with water and covered with a drop of 0.1 mg mL^{-1} BSA in 50 mM PBS for 30 min. After a final rinsing in 50 mM PBS, the gate was ready for the sensing measurements.

Electrochemical impedance spectroscopy measurements to characterize the gate electrode functionalization were performed in 5 mM K$_3$[Fe(CN)$_6$] and 1 M KCl at an ac voltage amplitude of 10 mV and dc potential of 0.26 V, in a frequency range from 0.1 Hz–10 kHz. The electrode imaginary (Z'') and real (Z') electrochemical impedance response were recorded. A CH Instrument potentiostat 760c model was used for the EIS, which was carried out using a three-electrode cell. The gate electrode was used as a working electrode, whereas a Pt wire and an Ag/AgCl electrode (Elbatech, Livorno Italy) were employed as counter electrode and

reference electrode , respectively. The Au gate electrodes were cleaned by rinsing with water and covering with a drop of H$_2$SO$_4$ 1 M for 1 h prior to the functionalization steps.

The R_{ET} and C_{DL} values had been obtained from the Nyquist plots, by fitting a Randles circuit, with a further R/CPE (resistance/constant phase element) component in-series, to model the initial semi-circle, due to the electrode complex structure. The fitting was performed with EIS Spectrum Analyzer software free software.

The electrochemically active surface area of the gate electrodes had been determined by solving the Randles–Sevcik equation on the peak currents obtained from cyclic voltammetry (CV) in 5 mM K$_3$[Fe(CN)$_6$], 1 M KCl, at 50 mV s^{-1}.

Device Electrical Characterization: Electrical measurements were performed in a phosphate buffer solution (PBS 50 mM, BSA 0.1 mg mL^{-1}, pH 7.4). Source, drain, and gate electrodes were connected to an Agilent B2902A Source Measure Unit. All measurements were carried out at room temperature inside a Faraday cage. Gate electrodes were incubated ex situ in solutions containing increasing [ATI] and rinsed with PBS before performing electrical measurements for 15 min. The device transfer characteristics were recorded by sweeping the gate-source voltage (V_{GS}) from −0.3 to 0.3 V while keeping the drain-source voltage (V_{DS}) constant at 50 mV. V_{GS} was limited to $|V_{GS}|<0.3$ V to avoid possible faradaic processes and keep the leakage current $I_{GS} < 1\% I_{DS}$ the source-drain current. After each step of functionalization and sensing, the devices were measured until stabilization that was assumed to be attained when the last five transfer curves were completely superimposable. The rGO-EGTs present a device-to-device variability in terms of charge neutrality point (0.05 V ±0 07 V) and overall current, the latter being always in the range of a few µA. A comparable variability is observed for the devices after gate functionalization, with a V_{CNP} of −0.13 ± 0.06 V.

The theoretical LOD was calculated according to its definition, i.e., minimum concentration whose current exceeds three times the standard deviation from the mean value of the current value acquired for [ATI] = 0 M.[43]

Supporting Information

Supporting Information is available from the Wiley Online Library or from the author.

Acknowledgements

Conflict of Interest

The authors declare no conflict of interest.

Data Availability Statement

The data that support the findings of this study are openly available in Zenodo at https://doi.org/10.5281/zenodo.8138121.

[1] L. S. Winterfield, A. Menter, *Dermatol. Ther.* **2004**, *17*, 409.

[2] D. M. Knight, H. Trinh, J. Le, S. Siegel, D. Shealy, M. Mcdonough, B. Scallon, M. A. Moore, J. Vilcek, P. Daddona, J. Ghrayeb, *Mol. Immunol.* **1993**, *30*, 1443.

[3] S. V. Onrust, H. M. Lamb, *BioDrugs* **1998**, *10*, 397.

[4] D. I. Jang, A. H. Lee, H. Y. Shin, H. R. Song, J. H. Park, T. B. Kang, S. R. Lee, S. H. Yang, *Int. J. Mol. Sci.* **2021**, *22*, 1.

[5] B. Gorovits, D. J. Baltrukonis, I. Bhattacharya, M. A. Birchler, D. Finco, D. Sikkema, M. S. Vincent, S. Lula, L. Marshall, T. P. Hickling, *Clin. Exp. Immunol.* **2018**, *192*, 348.

[6] J. Lu, T. Van Stappen, D. Spasic, F. Delport, S. Vermeire, A. Gils, J. Lammertyn, *Biosens. Bioelectron.* **2016**, *79*, 173.

[7] K. L. Thoren, B. Pasi, J. C. Delgado, A. H. B. Wu, K. L. Lynch, *J. Appl. Lab. Med. An AACC Publ.* **2018**, *2*, 725.

[8] K. P. Pratt, *Antibodies* **2018**, *7*, 19.

[9] M. Sensi, M. Berto, S. Gentile, M. Pinti, A. Conti, G. Pellacani, C. Salvarani, A. Cossarizza, C. A. Bortolotti, F. Biscarini, *Chem. Commun.* **2021**, *57*, 367.

[10] M. Selvaraj, P. Greco, M. Sensi, G. D. Saygin, N. Bellassai, R. D'Agata, G. Spoto, F. Biscarini, *Biosens. Bioelectron.* **2021**, *182*, 113144.

[11] M. Galliani, C. Diacci, M. Berto, M. Sensi, V. Beni, M. Berggren, M. Borsari, D. T. Simon, F. Biscarini, C. A. Bortolotti, *Adv. Mater. Interfaces* **2020**, *7*, 2001218.

[12] M. Berto, M. Di Giosia, M. Giordani, M. Sensi, F. Valle, A. Alessandrini, C. Menozzi, A. Cantelli, G. C. Gazzadi, F. Zerbetto, M. Calvaresi, F. Biscarini, C. A. Bortolotti, *Adv. Electron. Mater.* **2021**, *7*, 2001114.

[13] E. Macchia, K. Manoli, B. Holzer, C. Di Franco, M. Ghittorelli, F. Torricelli, D. Alberga, G. F. Mangiatordi, G. Palazzo, G. Scamarcio, L. Torsi, *Nat. Commun.* **2018**, *9*, 3223.

[14] Q. He, S. Wu, Z. Yin, H. Zhang, *Chem. Sci.* **2012**, *3*, 1764.

[15] P. Suvarnaphaet, S. Pechprasarn, *Sensors* **2017**, *17*, 2160.

[16] C. Reiner-Rozman, M. Larisika, C. Nowak, W. Knoll, *Biosens. Bioelectron.* **2015**, *70*, 21.

[17] R. Hasler, C. Reiner-rozman, S. Fossati, P. Aspermair, J. Dostalek, S. Lee, M. Ib, J. Bintinger, W. Knoll, *ACS Sens.* **2022**, *7*, 504.

[18] L. Wang, X. Wang, Y. Wu, M. Guo, C. Gu, C. Dai, D. Kong, Y. Wang, C. Zhang, D. Qu, C. Fan, Y. Xie, Z. Zhu, Y. Liu, D. Wei, *Nat. Biomed. Eng.* **2022**, *6*, 276.

[19] S. Pei, H. M. Cheng, *Carbon N Y* **2012**, *50*, 3210.

[20] P. Aspermair, V. Mishyn, S. Szunerits, W. Knoll, *Methods in Enzymology* **2020**, *642*, 371.

[21] W. Fu, L. Jiang, E. P. van Geest, L. M. C. Lima, G. F. Schneider, *Adv. Mater.* **2017**, *29*, 1603610.

[22] Jang, H. J., Sui, X., Zhuang, W., Huang, X., Chen, M., Cai, X., Wang, Y., Ryu, B., Pu, H., Ankenbruck, N., Beavis, K., Huang, J., Chen, J., *ACS Appl. Mater. Interfaces* **2022**, *14*, 24187.

[23] X. Jin, H. Zhang, Y. T. Li, M. M. Xiao, Z. L. Zhang, D. W. Pang, G. Wong, Z. Y. Zhang, G. J. Zhang, *Microchim. Acta* **2019**, *186*, 223.

[24] C. Reiner-Rozman, C. Kotlowski, W. Knoll, *Biosensors* **2016**, *6*, 17.

[25] R. Furlan de Oliveira, P. A. Livio, V. Montes-García, S. Ippolito, M. Eredia, P. Fanjul-Bolado, M. B. González García, S. Casalini, P. Samorì, *Adv. Funct. Mater.* **2019**, *29*, 1905375.

[26] S. Vasilijević, G. Mattana, G. Anquetin, N. Battaglini, B. Piro, *Electrochim. Acta* **2021**, *371*, 137819.

[27] R. Hasler, C. Reiner-Rozman, S. Fossati, P. Aspermair, J. Dostalek, S. Lee, M. Ibáñez, J. Bintinger, W. Knoll, *ACS Sens.* **2022**, *7*, 504.

[28] R. Furlan de Oliveira, V. Montes-García, P. A. Livio, M. B. González-García, P. Fanjul-Bolado, S. Casalini, P. Samorì, *Small* **2022**, *18*, 2201861.

[29] H. Wang, Y. Wu, C. Cong, J. Shang, T. Yu, *ACS Nano* **2010**, *4*, 7221.

[30] E. J. Gumbel, *Ann. Math. Statist.* **1941**, *12*, 163.

[31] N. Lago, M. Buonomo, R. C. Hensel, F. Sedona, M. Sambi, S. Casalini, A. Cester, *IEEE Trans. Electron Devices* **2022**, *69*, 3192.

[32] T. C. Tsai, C. W. Liu, Y. C. Wu, N. A. P. Ondevilla, M. Osawa, H. C. Chang, *Colloids Surf., B* **2019**, *175*, 300.

[33] V. Quintano, A. Kovtun, F. Biscarini, F. Liscio, A. Liscio, V. Palermo, *Nanoscale Adv* **2021**, *3*, 353.

[34] G. Palazzo, D. De Tullio, M. Magliulo, A. Mallardi, F. Intranuovo, M. Y. Mulla, P. Favia, I. Vikholm-Lundin, L. Torsi, *Adv. Mater.* **2015**, *27*, 911.

[35] M. Beeg, A. Nobili, B. Orsini, F. Rogai, D. Gilardi, G. Fiorino, S. Danese, M. Salmona, S. Garattini, M. Gobbi, *Sci. Rep.* **2019**, *9*, 2064.

[36] D. Shealy, A. Cai, K. Staquet, A. Baker, E. R. Lacy, L. Johns, O. Vafa, G. Gunn, S. Tam, S. Sague, D. Wang, M. Brigham-Burke, P. Dalmonte, E. Emmell, B. Pikounis, P. J. Bugelski, H. Zhou, B. Scallon, J. Giles-Komar, *mAbs* **2010**, *2*, 428.

[37] P. A. Manco Urbina, M. Berto, P. Greco, M. Sensi, S. Borghi, M. Borsari, C. A. Bortolotti, F. Biscarini, *J. Mater. Chem. C* **2021**, *9*, 10965.

[38] S. Demuru, C. H. Huang, K. Parvez, R. Worsley, G. Mattana, B. Piro, V. Noël, C. Casiraghi, D. Briand, *ACS Appl. Nano Mater.* **2022**, *5*, 1664.

[39] V. Parkula, M. Berto, C. Diacci, B. Patrahau, M. Di Lauro, A. Kovtun, A. Liscio, M. Sensi, P. Samorì, P. Greco, C. A. Bortolotti, F. Biscarini, *Anal. Chem.* **2020**, *92*, 9330.

[40] M. Sensi, G. Migatti, V. Beni, T. M. D'Alvise, T. Weil, M. Berto, P. Greco, C. Imbriano, F. Biscarini, C. A. Bortolotti, *Macromol. Mater. Eng.* **2022**, *307*, 2100880.

[41] E. Macchia, F. Torricelli, P. Bollella, L. Sarcina, A. Tricase, C. Di Franco, R. Österbacka, Z. M. Kovács-Vajna, G. Scamarcio, L. Torsi, *Chem. Rev.* **2022**, *122*, 4636.

[42] A. Goyon, M. Excoffier, M. C. Janin-Bussat, B. Bobaly, S. Fekete, D. Guillarme, A. Beck, *J. Chromatogr. B: Anal. Technol. Biomed. Life Sci.* **2017**, *1065–1066*, 119.

[43] A. G. González, M. Á.n. Herrador, *TrAC, Trends in Anal. Chem.* **2007**, *26*, 227.